Author's Accepted Manuscript

www.elsevier.com/locate/csr

Effects of Wave-Current Interaction on Storm Surge in the Taiwan Strait: Insights from Typhoon Morakot

Xiaolong Yu, Weiran Pan, Xiangjing Zheng, Shenjie Zhou, Xiaoqin Tao

PII: S0278-4343(17)30135-8
DOI: http://dx.doi.org/10.1016/j.csr.2017.08.009
Reference: CSR3651

To appear in: *Continental Shelf Research*

Received date: 26 March 2017
Revised date: 24 July 2017
Accepted date: 16 August 2017

Cite this article as: Xiaolong Yu, Weiran Pan, Xiangjing Zheng, Shenjie Zhou and Xiaoqin Tao, Effects of Wave-Current Interaction on Storm Surge in the Taiwan Strait: Insights from Typhoon Morakot, *Continental Shelf Research,* http://dx.doi.org/10.1016/j.csr.2017.08.009

This is a PDF file of an unedited manuscript that has been accepted for publication. As a service to our customers we are providing this early version of the manuscript. The manuscript will undergo copyediting, typesetting, and review of the resulting galley proof before it is published in its final citable form. Please note that during the production process errors may be discovered which could affect the content, and all legal disclaimers that apply to the journal pertain.

ACCEPTED MANUSCRIPT

Effects of Wave-Current Interaction on Storm Surge in the Taiwan Strait: Insights from Typhoon Morakot

Xiaolong Yu[a], Weiran Pan[b]*, Xiangjing Zheng[c], Shenjie Zhou[d], Xiaoqin Tao[b]

[a]Department of Ocean and Earth Sciences, University of Southampton, UK

[b]Department of Physical Oceanography, College of Ocean and Earth Sciences, Xiamen University, Xiamen, China

[c]Fujian Marine Forecasts, Fuzhou, China

[d]Centre for Ocean and Atmospheric Sciences, School of Environmental Sciences, University of East Anglia, Norwich, UK

Accepted manuscript

* *Corresponding author address*: Weiran Pan, Department of Physical Oceanography, College of Ocean and Earth Sciences, Xiamen University, Xiamen, China.

E-mail: panwr00@sina.com

ACCEPTED MANUSCRIPT

Abstract

The effects of wave-current interaction on storm surge are investigated by a two-dimensional wave-current coupling model through simulations of Typhoon Morakot in the Taiwan Strait. The results show that wind wave and slope of sea floor govern wave setup modulations within the nearshore surf zone. Wave setup during Morakot can contribute up to 24% of the total storm surge with a maximum value of 0.28 m. The large wave setup commonly coincides with enhanced radiation stress gradient, which is itself associated with transfer of wave momentum flux. Water levels are to leading order in modulating significant wave height inside the estuary. High water levels due to tidal change and storm surge stabilize the wind wave and decay wave breaking. Outside of the estuary, waves are mainly affected by the current-induced modification of wind energy input to the wave generation. By comparing the observed significant wave height and water level with the results from uncoupled and coupled simulations, the latter shows a better agreement with the observations. It suggests that wave-current interaction plays an important role in determining the extreme storm surge and wave height in the study area and should not be neglected in a typhoon forecast.

Key words: Typhoon Morakot, wave-current interaction, wave setup, radiation stress gradient.

Accepted manuscript

ACCEPTED MANUSCRIPT

1. Introduction

Tide-surge interaction is now recognized to cause limitations for numerical model to reproduce observed changes in mean water level under extreme weather conditions, especially at surf zones. Wave setup or setdown, typically arising from wave breaking, may be one mechanism that explains this discrepancy (Roland et al., 2009; Kim et al., 2010; Dietrich et al., 2011; Brown et al., 2013; Feng et al., 2016). Radiation stress serves as reservoirs of momentum flux between surface waves and underlying ocean currents, and is proportional to the wave energy density (Longuet-Higgins and Stewart, 1964; Smith 2006). The transfer of momentum flux from wind waves to water column is more evident when waves propagate from deep to shallow water, essentially by the gradients of radiation stress (Longuet-Higgins and Stewart, 1962). Water levels and currents have, in turn, a profound effect on wave height through distinct mechanisms. In the nearshore area, significant wave height (SWH) is strongly influenced by time-varying water depth (Bolaños et al., 2014). Ocean currents accelerate or decelerate the energy transferred from surface winds to surface waves outside the estuary, depending on the orientation of the current and the waves (Gonzalez, 1984; Wolf and Prandle, 1999; Hopkins et al., 2016). The wave-current interaction depends on many factors, including continental shelf geometry (Resio and Westerink, 2008), bathymetry (Raubenheimer et al., 2001), coastal morphology (Malhadas et al., 2009) and the path of hurricanes or typhoons (Feng et al., 2012).

The Taiwan Strait (TS) is located in the western Pacific Ocean at the intersection between the East China Sea (ECS) and the South China Sea (SCS), and is characterized by very strong tides and complex bottom topography (Hong et al., 2011). On average, 7.8 typhoons per year hit this important transition region of the two marginal seas, causing severe economic damage in both Mainland China and

Accepted manuscript

Taiwan (Cai et al., 2009). For example, in Fujian province of China (Fig. 1), storm surges and coastal flooding caused about US$ 18.10 billion direct economic losses and 1,229 fatalities from 1989 to 2014 (Fang et al., 2017). A better understanding of storm surge processes is therefore important. Previous studies have focused on tide-surge interaction in the TS (Zhang et al., 2010; Liu et al., 2016), while the effects of wave-current interaction during storm surges remain relatively understudied.

Here we examine the case of Typhoon Morakot (2009), with a key focus on the role of wave-current interaction (based on radiation stress theory in Longuet-Higgins and Stewart, 1962) in the nearshore areas near Fujian. Note that, in this article, our definition of current simply refers to tidal and surge-induced currents. The outline of the paper is as follows. In-situ observations and model setup are introduced in Section 2. Section 3 contains model validation. Section 4 includes a summary of the simulation results and a discussion of the effects of wave-current interaction during Typhoon Morakot. We present our conclusions in Section 5.

Accepted manuscript

2. Methods

2.1. Typhoon Morakot

The moving path of Typhoon Morakot (data from the China Meteorological Administration) is shown in Fig. 1. Morakot formed in the northwestern Pacific, northeast of the Philippines (21.2°N, 135.6°E), at 0200 UTC 4 August 2009, with an initial maximum wind speed of 18 m/s and central pressure of 994 hPa. It attained to the regulating strength of a typhoon at 1400 UTC 5 August and moved west towards Taiwan. Morakot made the first landfall on the east coast of Taiwan around 0000 UTC 8 August with maximum wind speed exceeding 30 m/s, and then turned northward around 0500 UTC 8 August. The Morakot eye moved into the TS at 0900

UTC 8 August and made its second landfall on the west coast of Fujian 31 hours later, around 1600 UTC 9 August.

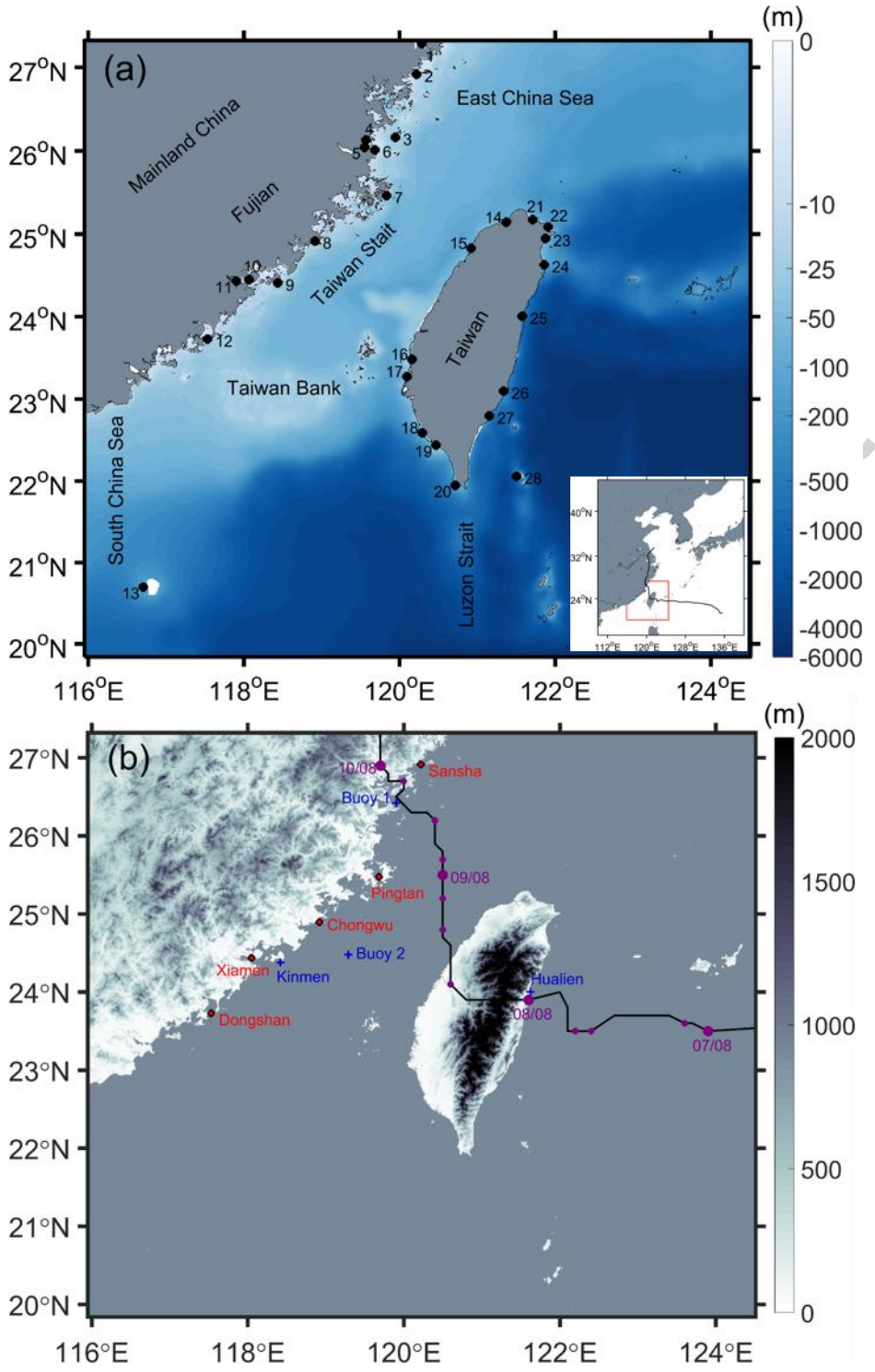

Fig. 1. (a) The bathymetry of the model domain. Twenty-eight tide-gauge stations used for validation of harmonic constants are marked with black dots. Inset map shows the Taiwan Strait and its adjacent region, with the path of Typhoon Morakot in

August 2009. The model domain is within the red box. (b) Schematic representation of land topographic features of the model domain with name markers of the locations of tide-gauge stations, buoys and meteorological stations. The path of Morakot is shown as a black line. Buoys 1, 2 and two meteorological stations used for validation of wind speed and significant wave height are shown with blue crosses. The five tide-gauge stations used for validation of water levels are shown with red dots. The ocean is coloured light grey.

2.2. In-situ observations

The harmonic constants of four major tidal constituents (M_2, S_2, K_1, O_1), at 28 tide-gauge stations (Fig. 1a), were computed using harmonic analysis (Pawlowicz et al., 2002) from the sea level data provided by the State Oceanic Administration of China and Taiwan's Central Weather Bureau. Two waverider buoys (Fig. 1b), both equipped with a meteorological package, measured SWH and wind speed. Buoys 1 and 2 were operated by Xiamen University and National Central University of Taiwan, respectively. Wind and wave measurements at two meteorological stations (Hualien, Kinmen) are used to complement the buoy data. Finally, five float type tide-gauge stations operated by the State Oceanic Administration of China along the Fujian coast (Fig. 1b), obtained water level observations during Morakot.

In the following validation section (Section 3), all the aforementioned in-situ observations will be used to validate models. The results from dynamical interest regions only (Sansha, Pingtan, Chongwu, Buoys 1 and 2) are discussed in Section 4.

2.3. Model domain

Numerical simulations are based on a coupling of the ADCIRC circulation model and the SWAN wave model. The computational domain extends from 19.84°N to 27.32°N, and from 115.95°E to 124.51°E, encompassing the whole TS and adjacent

Accepted manuscript

ACCEPTED MANUSCRIPT

oceanic regions, from the southern part of the ECS to the northeastern part of the SCS (Fig. 1a). The unstructured mesh over the computational domain was generated by Surface Water Modeling System 10.1, including 28,100 computational nodes and 52,871 triangle units. Fine horizontal resolution of mesh in the range 0.7-2.5 km was applied to the surf zone, and relatively coarse mesh resolution of 2.5-36 km was applied in the TS and western Pacific regions to capture the generation of waves in deep water and their propagation onto the continental shelf. The simulations run from 4 August to 11 August, and the results from 7 August to 11 August are used in the present study.

The coastline was determined by the Global Self-Consistent Hierarchical High-resolution Geography Database (GSHHG), provided by National Oceanic and Atmospheric Administration (NOAA). To improve the accuracy of coastline along the Fujian Province of China, corrections were applied according to the nautical charts, published by China Maritime Safety Administration (CMSA). The bathymetry (Fig. 1a) was obtained from the NOAA ETOPO2 dataset, and corrections were applied to the nearshore zone from the tidal information panel. The minimum water depth was set to be 4 m. The moving speed of typhoon eye and pressure data during Morakot were obtained from the CMA Tropical Cyclone Data Center (http://tcdata.typhoon.gov.cn/en/).

Accepted manuscript

2.4. Model Implementation

Here, we employed a simple one-way coupling method (Huang et al., 2010). Three steps are needed. First, the ADCIRC is initiated and run with astronomic tidal and meteorological forcing to output water levels and currents. This run is denoted by 'ADCIRC only'. Second, the information of water levels and currents from run 'ADCIRC only', as well as the same meteorological forcing, is used as inputs to run

SWAN. Third, radiation stress gradients produced by SWAN, astronomic tidal and meteorological forcing are transferred back to ADCIRC, to obtain the coupled water levels and currents. This return-run is denoted by 'ADCIRC + SWAN'.

To do comparisons (Section 3), the SWAN driven by meteorological forcing is run alone, denoted by 'SWAN only'. Furthermore, another ADCIRC run is applied, only driven by astronomic tidal forcing at the open boundary. This run is denoted by 'ADCIRC tide', and the results are used in the validation of harmonic constants (Section 3.1) and co-tidal chart analyses (Section 4.1).

2.5. Wave-induced radiation stress

The essence of wave setup or setdown is well captured by the spatial gradient of radiation stress, which represents the transition of the momentum flux induced by wave breaking. The gradients of radiation stress are defined as,

$$F_x = -\frac{\partial S_{xx}}{\partial x} - \frac{\partial S_{xy}}{\partial y},\ F_y = -\frac{\partial S_{yx}}{\partial x} - \frac{\partial S_{yy}}{\partial y}, \quad (1)$$

where F_x and F_y denote the gradient of radiation stress in the x, y directions, respectively. Radiation stresses S_{xx}, S_{xy}, S_{yx} and S_{yy} are determined in terms of wave energy density spectrum from SWAN, and defined as,

$$S_{xx} = \rho g \int \left[n\cos^2\theta + n - \frac{1}{2} \right] E(\omega,\theta)\, d\omega d\theta,$$

$$S_{xy} = S_{yx} = \rho g \int n \sin\theta \cos\theta\, E(\omega,\theta)\, d\omega d\theta,$$

$$S_{yy} = \rho g \int \left[n\sin^2\theta + n - \frac{1}{2} \right] E(\omega,\theta)\, d\omega d\theta, \quad (2)$$

where ρ is the water density, g is the gravitational acceleration, n is the ratio of group velocity to phase velocity, $E(\omega,\theta)$ is the directional wave energy density spectrum, ω is the absolute frequency determined by the Doppler shifted dispersion relation, and θ is the spectral direction.

Accepted manuscript

ACCEPTED MANUSCRIPT

The governing equations in the ADCIRC and SWAN models are described in Dietrich et al. (2011). Note that the gradients of radiation stress (F_x and F_y) are included in the ADCIRC governing equations (i.e., the generalized wave continuity equation and vertically-integrated momentum equations) to obtain water levels and currents. In turn, the water levels and currents being passed to SWAN will update all the depth- and current-related terms in the action balance equation (e.g., depth- and current-induced refraction, the shifting of the relative frequency).

2.6. Meteorological forcing

Following Fujita (1952), the initial pressure profile of a typhoon is expressed as

$$P = P_\infty - (P_\infty - P_0)/\sqrt{1 + 2(r/R)^2}, \quad (3)$$

where P_∞ is the ambient pressure of the typhoon eye, P_0 is the central pressure of the typhoon eye, r is the distance between a grid and the typhoon eye and R is the function of maximum wind speed radius of a typhoon.

The wind field $\boldsymbol{W}$ can be expressed as

$$\boldsymbol{W} = c_1\boldsymbol{W_p} + c_2\boldsymbol{W_t}, \quad (4)$$

where c_1 and c_2 are the empirical coefficients (Fujii and Mitsuta 1986), $\boldsymbol{W_p}$ denotes the wind fields associated with surface pressure, and $\boldsymbol{W_t}$ denotes the wind fields caused by typhoon motion.

By assuming the gradient wind relation, we determine $\boldsymbol{W_p}$ as

$$\boldsymbol{W_p} = \left(\sqrt{\frac{f^2r^2}{4} + \frac{r}{\rho_a}\frac{\partial P}{\partial r}} - \frac{fr}{2}\right) \cdot \left(-sin(\phi + \beta)\,\vec{\imath},\ cos(\phi + \beta)\vec{\jmath}\right), \quad (5)$$

where f is the Coriolis parameter, ρ_a is the air density, ϕ represents the direction of the grid relative to the moving typhoon centre, β is the angle between gradient wind and sea surface wind, and $\vec{\imath}$ and $\vec{\jmath}$ are the unit vectors in the x, y directions, respectively.

Accepted manuscript

Following Miyazaki et al. (1961), $\boldsymbol{W_t}$ is defined as

$$\boldsymbol{W_t} = exp(\frac{-\pi r}{500000}) \cdot (V_x \vec{i}, V_y \vec{j}), \quad (6)$$

where V_x, V_y denote the velocity components of the typhoon motion in the x, y directions, respectively.

The geometry and land topography (Fig. 1b) have an impact on the structure of wind fields blowing through the TS (Chang et al., 1993; Shimada et al., 2016). Enhanced northeasterly along-strait winds associated with tropical cyclones are often observed (Zhang et al. 2009; Wei, 2015). Briefly, following method in Chen (2006), we introduced a weighted factor, which takes into account bathymetry, the width of the TS, land topography and the locations of the typhoon eye, to improve the accuracy of wind simulations. The weighted factor is generally larger than O (1) in the TS in our simulations. Finally, we ignore the background wind forcing in this study, since it is negligible compared to the typhoon wind field.

2.7. Oceanic boundary forcing

Tidal forcing at the ocean lateral boundary, including eight major tidal constituents (M_2, S_2, N_2, K_2, K_1, O_1, P_1, Q_1), is derived from the OSU Tidal Inverse System (OTIS, Egbert and Erofeeva, 2002). The non-slip boundary condition was applied over the land boundary. Water levels and velocities at all computational nodes were set to be zero at initialization. Bottom friction effect is represented by the quadratic bottom friction stress formula with drag coefficient of 0.0025.

Accepted manuscript

ACCEPTED MANUSCRIPT

3. Model validation

3.1. Tide validation

The modeled harmonic constants (amplitude and phase of M_2, S_2, K_1 and O_1) agree well with those estimated from observations (Fig. 2), with best-fit slopes of 0.95-1.10 and statistically significant correlation coefficients exceeding 0.90. The mean absolute error of harmonic constants of four major tidal constituents is in the range of 1.9 cm (O_1) to 5.7 cm (M_2) for amplitude and 3.25° (O_1) to 4.95° (S_2) for phase. Simulation results have a better agreement with observations located on the west bank of TS than the east bank, most likely due to higher horizontal resolution near the Fujian coastal region.

Accepted manuscript

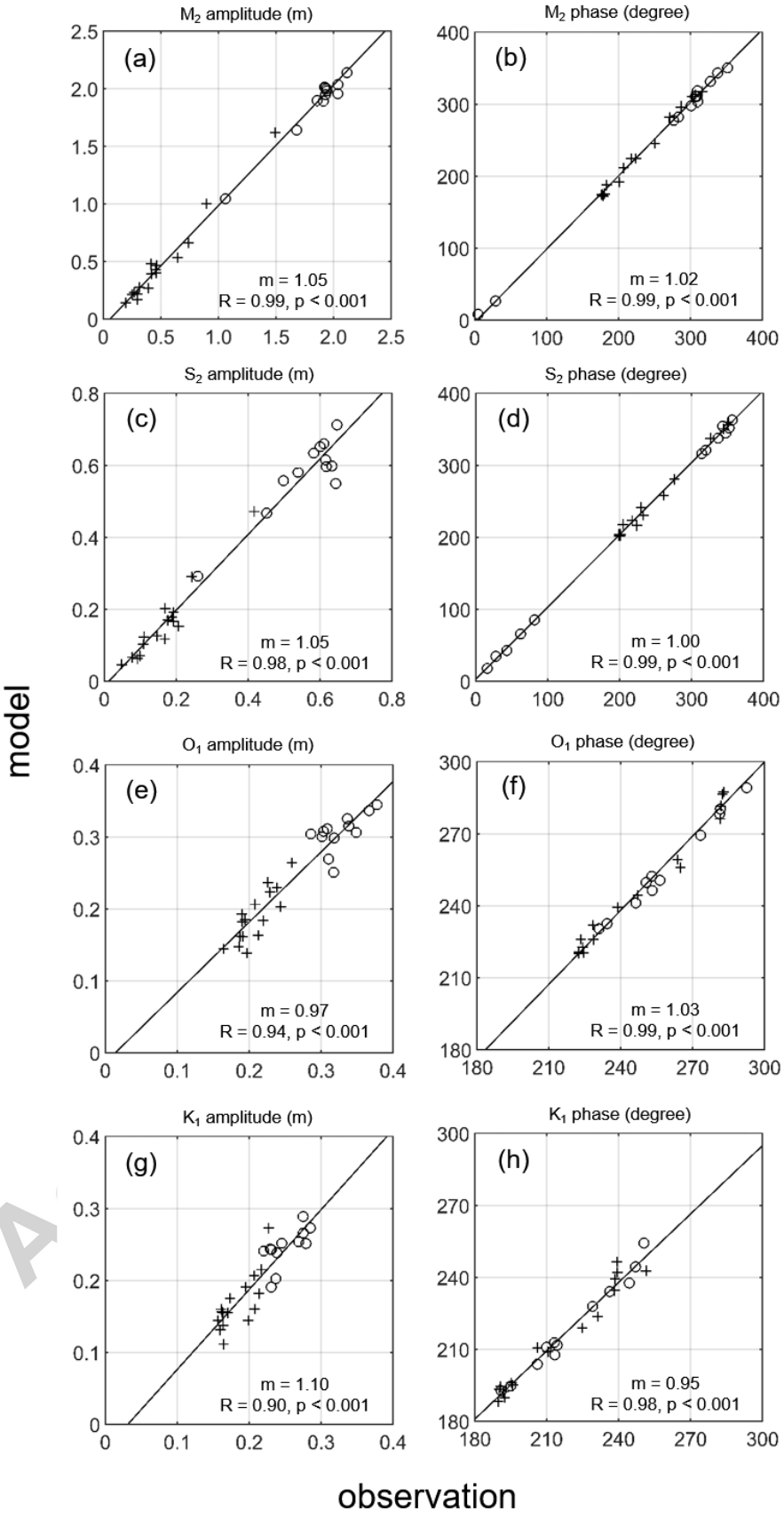
M2 amplitude (m)
(a)
m = 1.05
R = 0.99, p < 0.001
M2 phase (degree)
(b)
m = 1.02
R = 0.99, p < 0.001
S2 amplitude (m)
(c)
m = 1.05
R = 0.98, p < 0.001
S2 phase (degree)
(d)
m = 1.00
R = 0.99, p < 0.001
O1 amplitude (m)
(e)
m = 0.97
R = 0.94, p < 0.001
O1 phase (degree)
(f)
m = 1.03
R = 0.99, p < 0.001
K1 amplitude (m)
(g)
m = 1.10
R = 0.90, p < 0.001
K1 phase (degree)
(h)
m = 0.95
R = 0.98, p < 0.001
model
observation

ACCEPTED MANUSCRIPT

Fig. 2. The comparison of modeled tidal amplitude (left panel) and phase (right panel) with observations at the twenty-eight tide-gauge stations for (a-b) M_2, (c-d) S_2, (e-f) K_1 and (g-h) O_1 tides. Stations 1-12 are shown with black circles, and the rest (13-28) are shown with black plus signs. The lines of best fit are shown with black solid lines with the slope m identified.

3.2. Wind and wave validation

The overall modeled wind speed matches well with measurements throughout the time series (Figs. 3a-d). The mean absolute error of wind speed at Hualien, Buoy 1, Buoy 2 and Kinmen stations are 5.88 m/s, 3.58 m/s, 3.35 m/s and 2.15 m/s, respectively. It is noted that modeled wind speeds reflect the observed peaks well, with differences all less than 5 m/s.

SWH values estimated from model runs 'SWAN only' and 'ADCIRC + SWAN' are compared to observations in Figs. 3e-h. By including the effects of water levels and currents, 'ADCIRC + SWAN' run showed a more consistent pattern with observations than the 'SWAN only' run. For example, the correlation coefficient increased from 0.85 to 0.90 at Buoy 1 and from 0.82 to 0.84 at Buoy 2. The simulated SWH at Hualien also matches well with the observed SWH. Further, the observed SWH (< 3 m) at Kinmen are small compared with other three stations as Kinmen is far from the Morakot path. However, in our simulations SWH at Kinmen is overestimated during the storm (with a maximum value of 4 m) and underestimated after the storm.

Accepted manuscript

ACCEPTED MANUSCRIPT

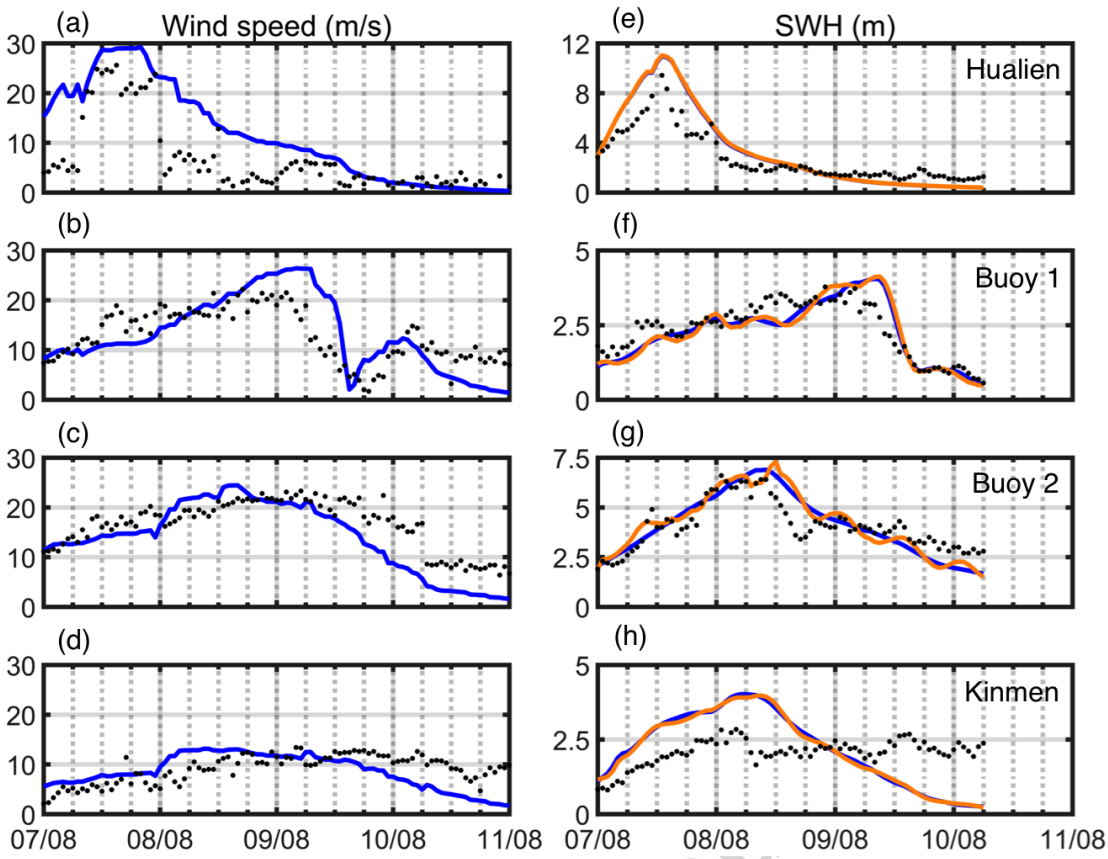

Fig. 3. The comparison of modeled wind speed (left panel) and significant wave height (right panel) with observations at (a and e) Hualien station, (b and f) Buoy 1, (c and g) Buoy 2 and (d and h) Kinmen station. The observed data are shown with black dots. The blue lines on the left panel denote modeled wind speed. The blue and orange lines on the right panel denote the model results from 'SWAN only' and 'ADCIRC + SWAN', respectively.

Accepted manu

3.3. Water level validation

The modeled water levels have been validated by direct observations collected at five tide-gauge stations. The coupled water levels obtained from the run 'ADCIRC + SWAN' agreed well with observed water levels (Fig. 4). Including radiation stress gradient in the run 'ADCIRC + SWAN' has improved the water levels to match the observed peak values and the average absolute error compared to the 'ADCIRC only'.

This feature is more obvious at stations near the track (e.g., the mean absolute error decreased from 0.38 m to 0.33 m at Sansha and from 0.26 m to 0.20 m at Pingtan). At stations distant from the Morakot track (e.g., Xiamen, Dongshan), the water levels from model runs 'ADCIRC only' and 'ADCIRC + SWAN' were remarkably similar, indicating the negligible wave effects on the storm surge at these locations.

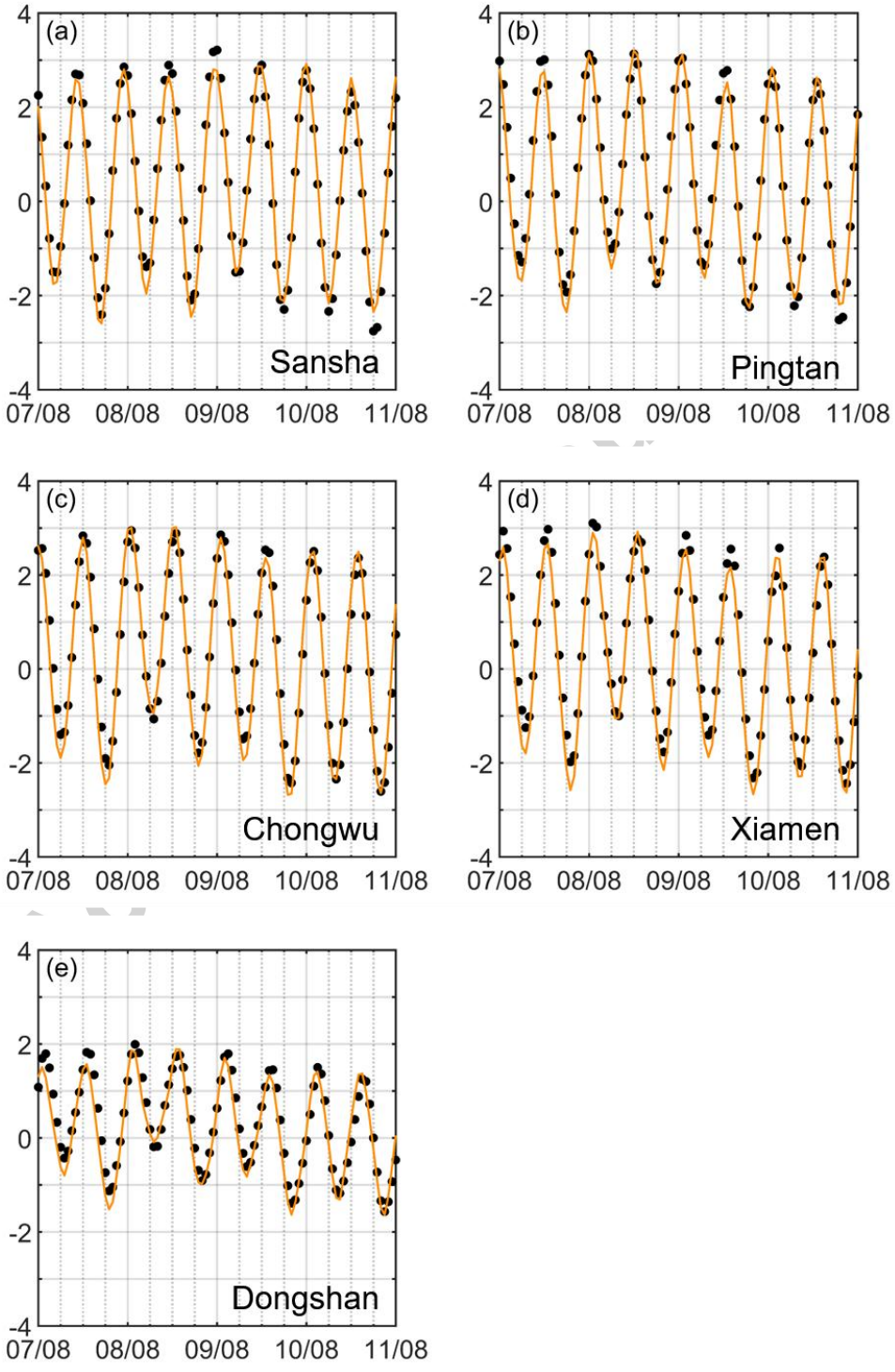

Fig. 4. The comparison of coupled water levels with observations at five tide-gauge stations. The observed data are shown with black dots, the modeled results from 'ADCIRC + SWAN' are shown with orange lines.

4. Results

4.1. Characterization of tidal waves in the TS

A key step in simulating the wave-current interaction during a typhoon is to obtain accurate tidal fields, especially in a tide-dominated region like the TS. The co-tidal charts of the semi-diurnal (M_2) and diurnal (K_1) tides in the TS are provided by Fig. 5. The general structure of co-amplitude and co-phase lines is consistent with previous numerical studies (Fang et al., 1999; Jan et al., 2004; Hu et al. 2010). The M_2 tide is the largest tidal constituent in the TS, with a range of amplitude from 0.4 to 2 m (Fig. 5a). It is visible as a southward-propagating Kelvin wave on the west bank of TS and a nearly standing wave near the southwestern coastal regions of Taiwan. The tidal wave propagation and reflection, shaped by the underlying abruptly deepened topography over south of the Taiwan Bank (Fig. 1a), might be the key contributor of the co-existence of two distinct waves in the TS (Jan et al., 2002; Jan et al., 2004; Yu et al., 2017). The large amplitude (~2 m) of M_2 tide is common from the middle section to the northern end of the TS, while abruptly decreasing occurs in the southern TS. In contrast, the K_1 tide appears as a single propagating wave, mostly aligned along the TS with a much smaller magnitude (0.2-0.32 m) (Fig. 5b). Both M_2 and K_1 tides exhibit enhanced amplitudes on the west bank of the TS (Fig. 2), as expected from Coriolis effects. This feature is also clearly seen by the amplitudes of M_2 and K_1 tides at 28 tide-gauge stations (vertical bars in Fig. 5) distributed on both sides of the TS.

Accepted manuscript

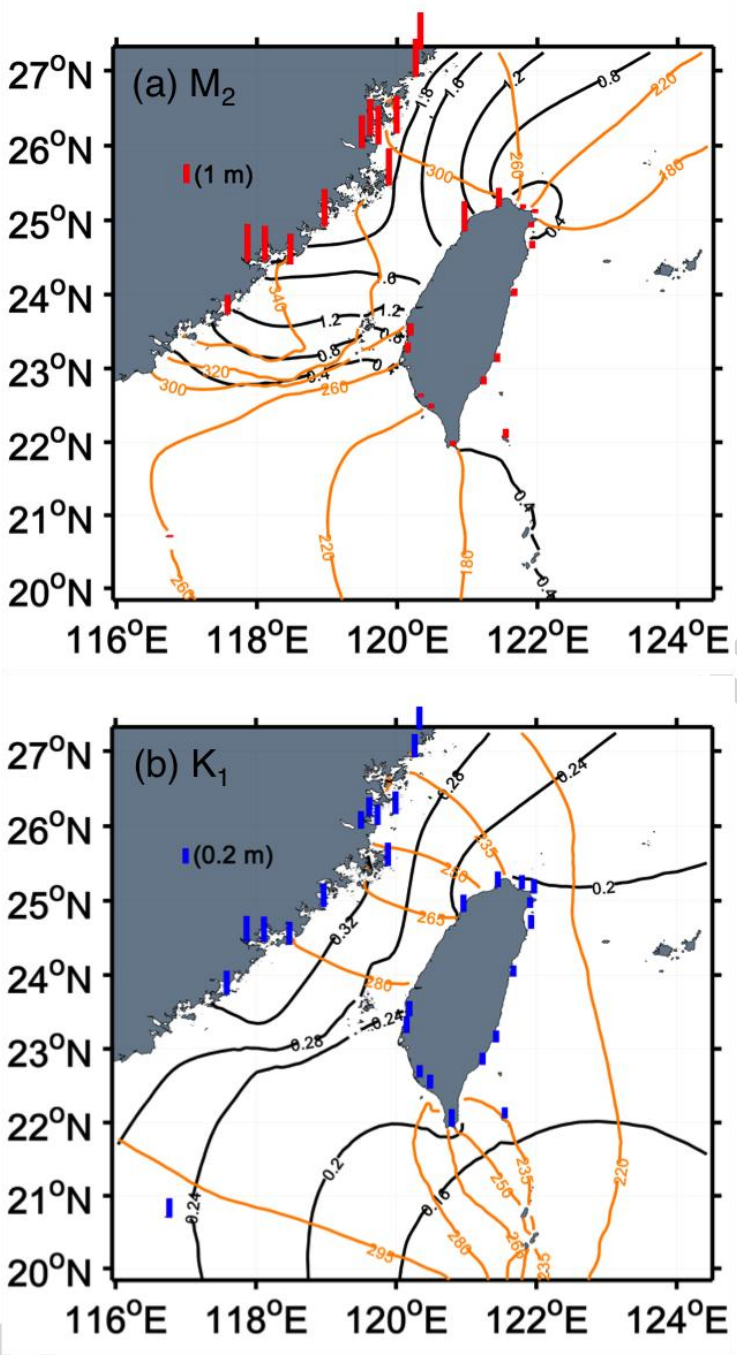

Fig. 5. Co-tidal chart for the (a) M_2 and (b) K_1 tides. The amplitude of the tide (black lines) is in metres and the tide phase (orange lines) is in degrees. Vertical bar represents the modeled amplitude at twenty-eight tide-gauge stations.

4.2. Wind and wave simulations

We next examine a series of simulation results at three time points: i) 1800 UTC 7 August (six hours before Morakot's landfall on Taiwan), ii) 1400 UTC 8 August (five hours after Morakot entered the TS) and iii) 1400 UTC 9 August (two hours before Morakot's landfall on Fujian).

The coupled SWH with wind fields in the model domain are shown in Figs. 6a-c. The striking feature of wind fields at 1800 UTC 7 August was the anti-clockwise winds centered at Morakot's eye, blowing a large portion of easterly winds against Hualien station, and winds aligned along the TS. The largest waves were generated near the Morakot's center, exceeding 10 m. Consistently, wind speeds at Hualien showed the most rapid increase on 7 August (Fig. 3a), with maximum observed value of 25 m/s at 1200 UTC 7 August, coincident with the occurrence of largest SWH, which was about 10 m (Fig. 3e).

In the TS, the modeled wind speed was of order 20 m/s, with SWH about 6 m. It is consistent with observed values at Buoy 2. Remarkably, the observed wind speed at Buoy 2 reached to about 20 m/s at the same time as Hualien (about nine hours before Morakot entered the TS), and remained uniformly strong at O (20 m/s) until the secondary peak of wind speed occurred at Buoy 1 (Figs. 3b and c). These persistently strong winds were largely due to the geometry effects of the TS. Our modified wind model captures this marked feature well (Fig. 3c).

Accepted manuscript

ACCEPTED MANUSCRIPT

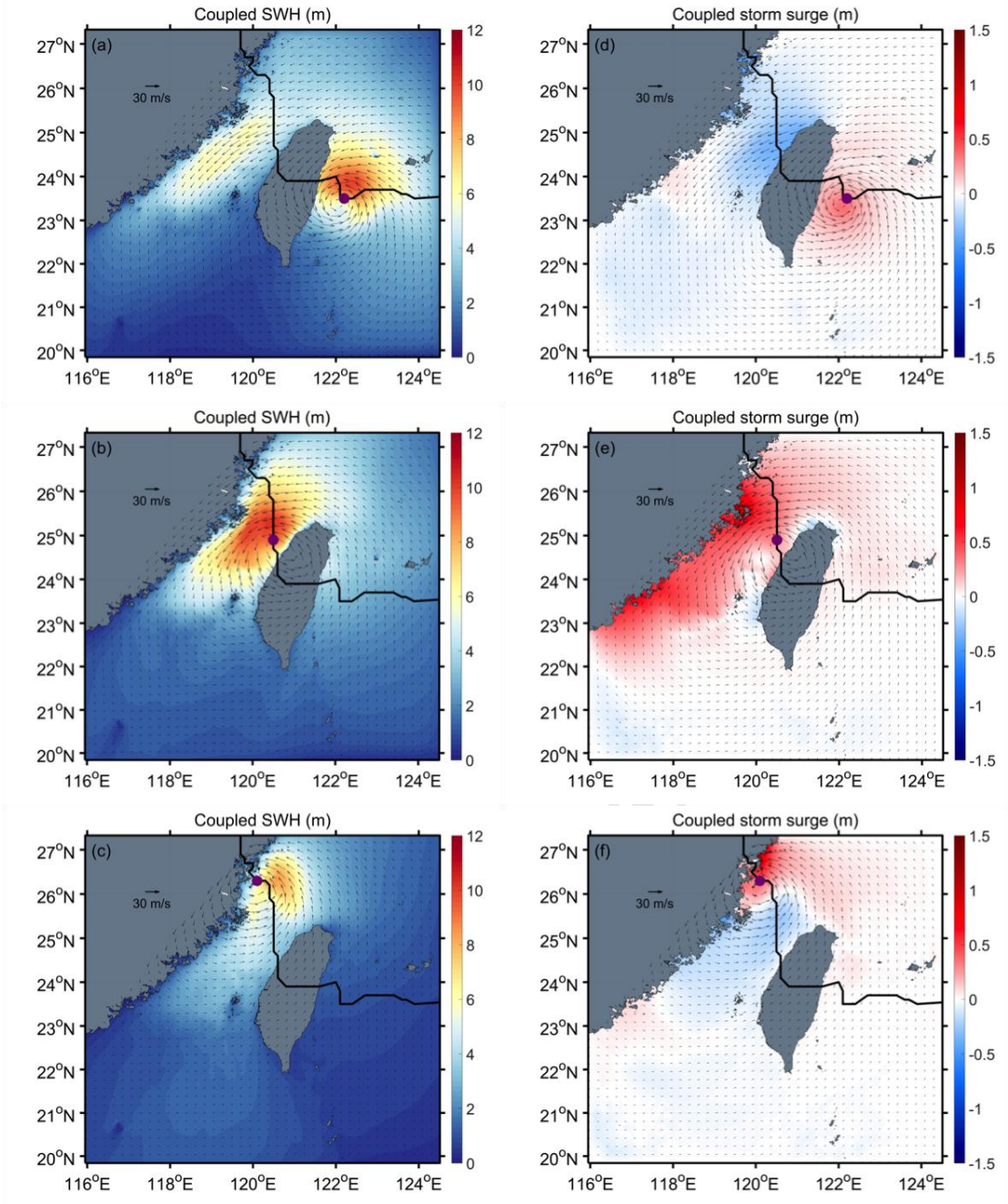

Fig. 6. Planar views of coupled SWH (left panel) and storm surge (right panel) during Morakot. The six panels correspond to the following times: (a and d) 1800 UTC 7 August 2009, (b and e) 1400 UTC 8 August 2009, (c and f) 1400 UTC 9 August 2009. Wind speed vectors are superimposed as black arrows. The path of Morakot is shown as a black line and the eye is represented by a purple dot.

At 1400 UTC 8 August, the largest waves were generated around the Morakot's center in the TS, and mainly propagated onto the west bank of the TS (Fig. 6b). The wind speed and SWH at Hualien decreased very quickly once Morakot had passed this region, with wind speed less than 10 m/s and SWH smaller than 1 m (Figs. 3a and e). The observed wind speed at Buoy 1 increased more gently compared to Hualien as Morakot entered the TS, peaking at 22 m/s around 0000 UTC 9 August (Fig. 3b). The SWH also attained a maximum value about 3.85 m at the same time. The observed SWH at Buoy 2 had a larger magnitude than Buoy 1, exceeding 6.5 m when Morakot entered the TS (Figs. 3c and g). After that, SWH at Buoy 2 steadily decreased to about 2.5 m at Morakot's landfall on Fujian.

Before Morakot's landfall on Fujian (Fig. 6c), the impact of Morakot on waves was mainly on the right-hand side of its path, where the SWH reached to about 6 m. In the majority of the TS regions, the wind speed was small and SWH decreased dramatically compared to Fig. 6b. However, a secondary peak of wind speed occurred at Buoy 1 about 11 hours after Morakot's landfall on Fujian (0300 UTC 10 August), whereas the SWH was small (about 1 m). This secondary peak is well reproduced in model results (Fig. 3b).

4.3. Storm surge and wave setup

Figs. 6d-f show the coupled storm surge in the TS, which is the difference in the water levels between runs 'ADCIRC tide' and 'ADCIRC + SWAN'. Generally, the storm surge during Morakot was widespread and large. A range of -0.5 to 1.5 m storm surge, driven by the meteorological forcing and wave momentum flux, can be seen in the TS. In particular, when Morakot entered the TS (Fig. 6e), the storm surge in most of the coastal region of Fujian was on the order of 1 m. Consistent with SWH in Fig.

Accepted manuscript

6c, the major storm surge was on the right-hand side of the Morakot path before its second landfall (Fig. 6f).

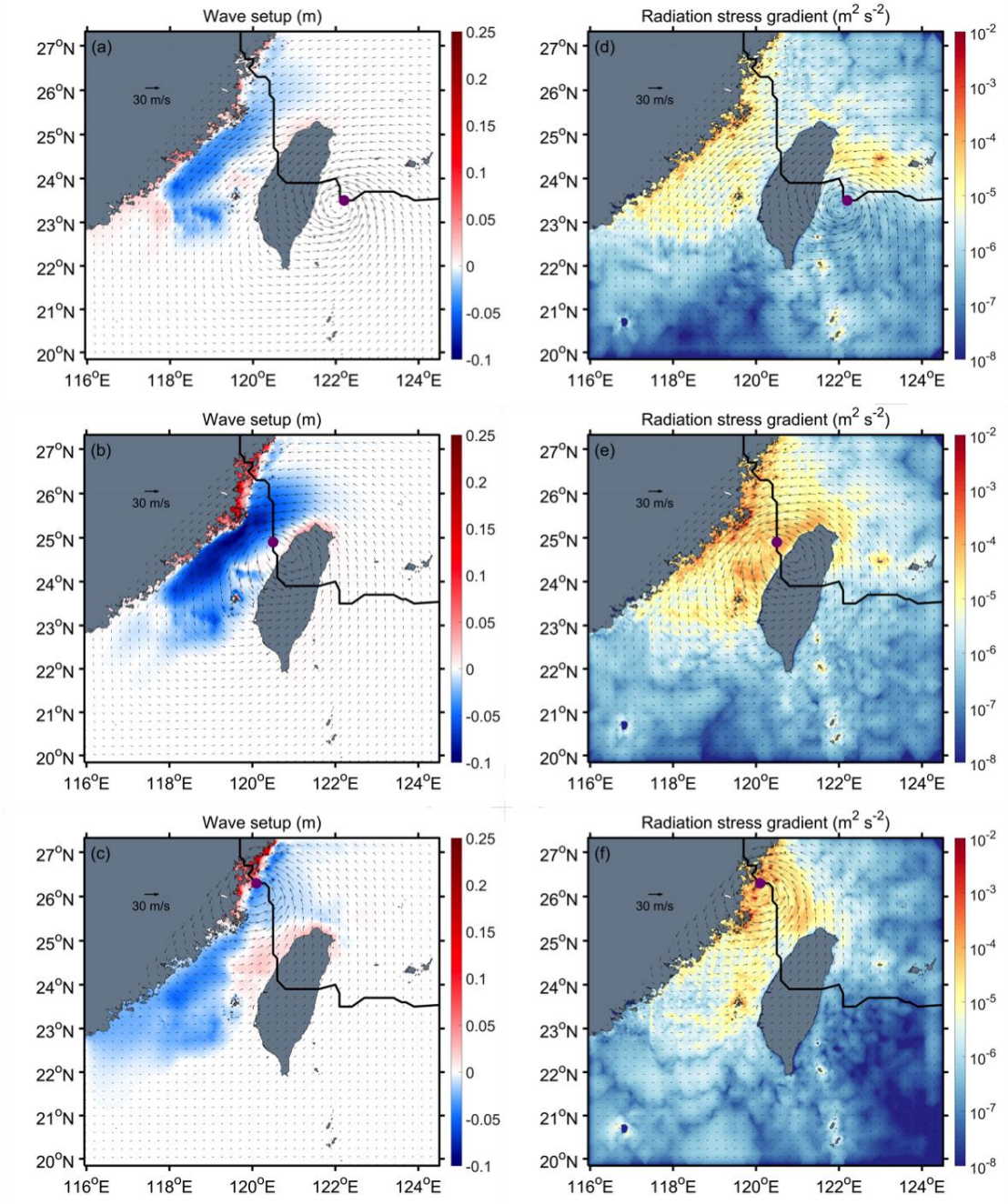

Fig. 7. Planar views of coupled wave setup (left panel) and radiation stress gradient (right panel) during Morakot. The six panels correspond to the following times: (a and d) 1800 UTC 7 August 2009, (b and e) 1400 UTC 8 August 2009, (c and f) 1400 UTC 9 August 2009. Wind speed vectors are superimposed as black arrows. The path of Morakot is shown as a black line and the eye is represented by a purple dot.

As waves propagate from the continental shelf into the shallow surf zone, radiation stress gradient is generated and induce wave setup. The wave setup is computed as the difference in the water levels between runs 'ADCIRC only' and 'ADCIRC + SWAN' (Figs. 7a-c). Wave setup gradually distributed in the nearshore areas with an enhancement on the right hand of Morakot path, while wave setdown distributed in most offshore areas. It is consistent with the setup nearshore and setdown offshore (Bowen et al., 1968; Olabarrieta et al., 2011). The mean wave setup in the TS was 0.04 m, with the largest values 0.28 m. In the nearshore area, wave setup is increasingly important. The wave setup associated with radiation stress gradient contributions ranged from 4% to 24% of the overall storm surge. The mean wave setdown was -0.03 m, while the largest setdown was about -0.10 m, approximately two times smaller than the wave setup peak value.

The radiation stress gradient throughout the TS was in the range of 10^{-5}-10^{-3} m^2 s^{-2} (Figs. 7d-f). In the nearshore surf zone, radiation stress gradient was intensified as waves shoaled and broke, with values on the order of 10^{-3} m^2 s^{-2}. Enhanced wave setup was common to regions of large radiation stress gradient, suggesting a causal relationship between the two variables.

4.4. Wave effects on storm surge

In the previous section, the wave setup induced by gradients of radiation stress is shown to be significant in the nearshore areas. We now have a closer look at the time series of wave setup and SWH at our dynamical interest regions (Fig. 8). This was achieved by confining the modeled results to 5 km × 5 km box centered on Sansha, Pingtan, Chongwu and Buoys 1, 2. The mean and standard deviation values are computed over each box.

Accepted manuscript

The wave setup varied significantly with time and areas (Fig. 8). The regions near the Morakot path (e.g., Sansha and Pingtan) had substantially larger magnitude than those relatively far from the path (e.g., Chongwu). The maximum wave setup (0.28 m) occurred to the east of the Pingtan at 1400 UTC 8 August, when waves of ~10 m propagated from north of the TS were breaking as the water depth shoals sharply. The wave setup broadly follows the trend of SWH in the nearshore areas (Figs. 8a-d). The wave setup is modest at times of weak SWH, but is elevated when large SWH propagates through the respective locations. SWH exhibits more high-frequency variability (e.g., M2 semi-diurnal tidal signal) than wave setup. To isolate wind-wave features from these tidal oscillations, a 12-hour time averaging is applied to SWH and wave setup, and scatter plots are used to illustrate correlations between different variables. We find that most of the enhanced wave setup periods coincide with large values of SWH (Fig. 9), as indicated by an overall strong correlation between SWH and wave setup inside the estuary. However, a somewhat different picture, in which the magnitude of wave setdown is proportional to the SWH, is found at Buoy 2. It suggests that wave setup and setdown are closely associated with offshore SWH, and the larger SWH, the larger wave setup inside the estuary and wave setdown outside the estuary.

Table 1 shows the time of occurrence of max wave setup and the corresponding wind-driven storm surge. Wind-driven storm surge is estimated by the differences in the water levels between runs ‘ADCIRC only’ and ‘ADCIRC tide’. The wave contribution to storm surge at Pingtan region might attain a maximum value about 24.0% of the instantaneously coupled storm surge. The contributions of wave setup at regions of Sansa, Chongwu and Buoy 1 were in the range of 6.9%-17.2%. Wave setdown occurred at Buoy 2, which was outside of the surf zones. Furthermore,

Accepted manuscript

negligible wave contribution to storm surge (< 4%) can be seen in the regions of Xiamen, Kinmen and Dongshan, which are far from the Morakot moving path.

The magnitude of wave setup is likely to be dynamically constrained by the slope of the sea floor (Resio and Westerink, 2008). Wave effects to storm surge in regions of steep slope are shown to be substantially larger than those in the gently sloping continental shelf (Funakioshi et al., 2008; Dietrich et al., 2010). To further link the wave setup to the slope of the sea floor in the TS, we next examine an appropriate scaling for wave setup (Resio and Westerink, 2008) $\Delta\zeta = L\,|\nabla_h F|/gh$, where $\Delta\zeta$ is the wave setup, $|\nabla_h F|$ is the magnitude of radiation stress gradient, and h is the mean water depth. For the TS, L = 180 km, h = 60 m and $|\nabla_h F|$ = 10^{-3} m^2 s^{-2}, predicts a wave setup of 0.3 m, which is consistent with the maximum value 0.28 m in our model. This scaling argument suggests that for the TS wave setup plays an important role in determining the extreme state of the local storm surge.

Accepted manuscript

ACCEPTED MANUSCRIPT

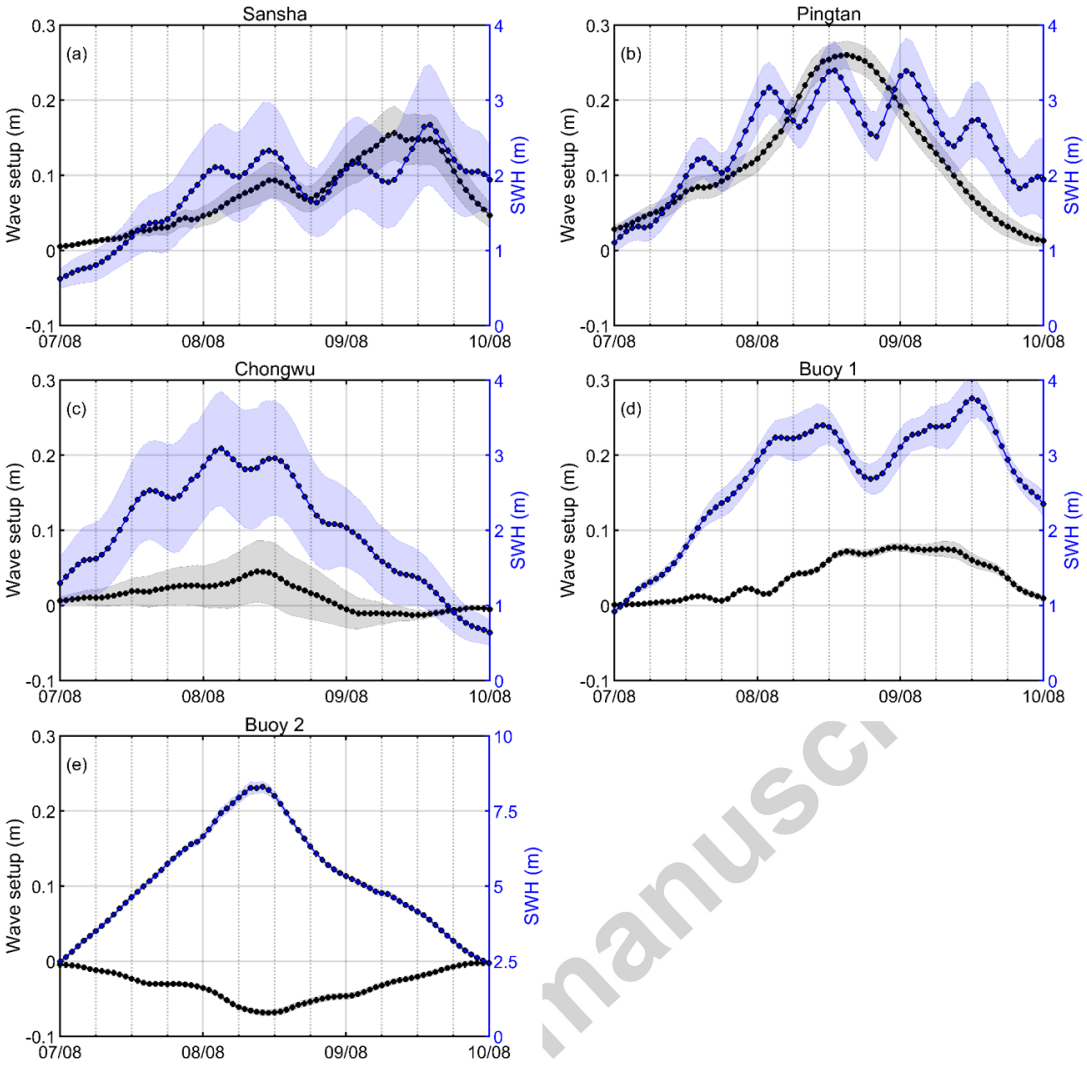

Fig. 8. Mean wave setup (black lines) and coupled SWH (blue lines) at regions of (a) Sansha, (b) Pingtan, (c) Chongwu, (d) Buoy 1 and (e) Buoy 2 during Morakot. The standard deviation is shown by the light shades.

Accepted manuscript

ACCEPTED MANUSCRIPT

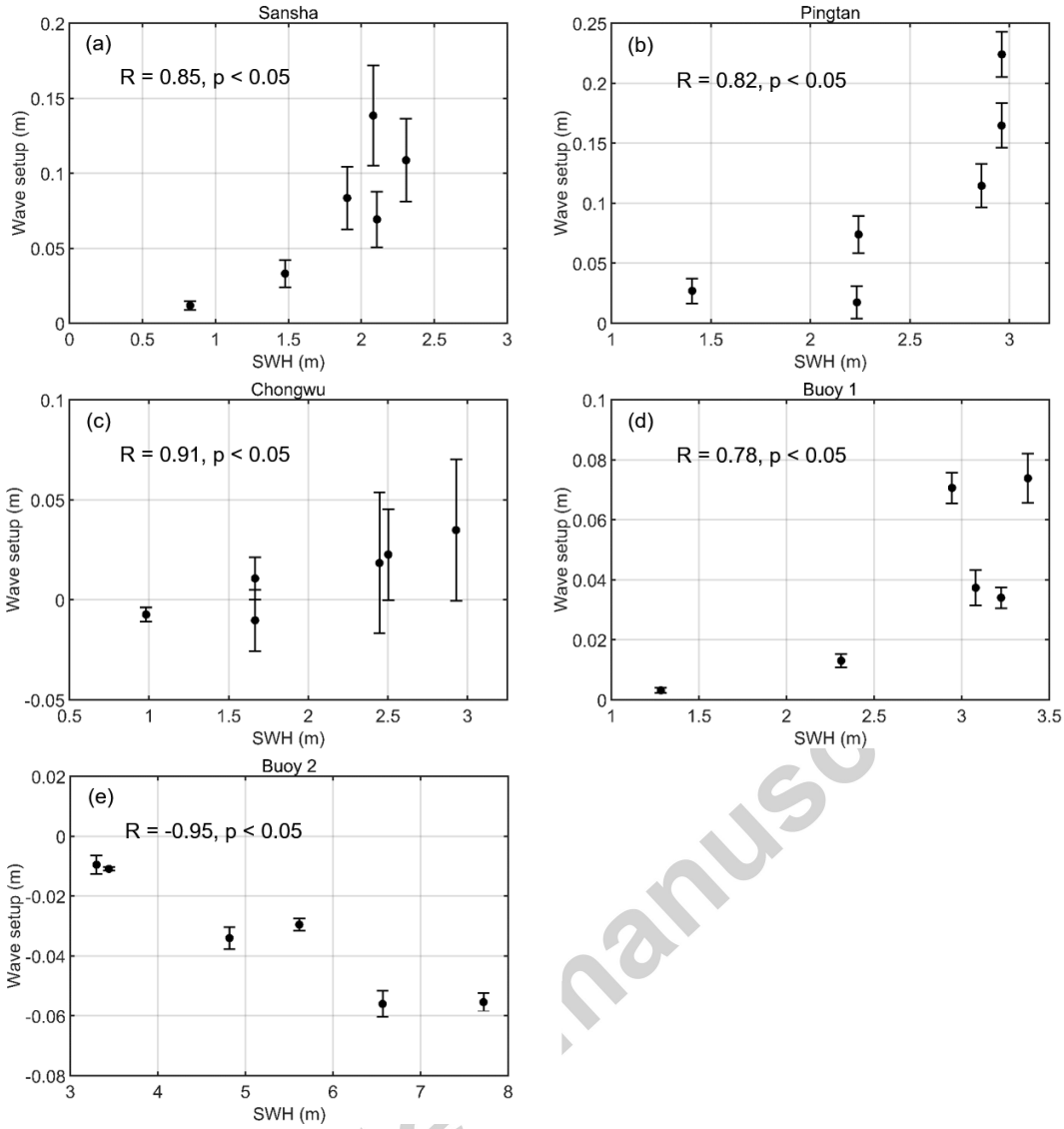

Fig. 9. Wave setup dependence on SWH at regions of (a) Sansha, (b) Pingtan, (c) Chongwu, (d) Buoy 1 and (e) Buoy 2 during Morakot. Fields are 12-hour averages, and the standard deviation computed for each box is illustrated by the vertical bars.

Accepted manuscript

ACCEPTED MANUSCRIPT

Table 1 The time of occurrence of max wave setup and the corresponding wind-driven storm surge.

Station	Time (YYYYMMDD)	Wave setup (m)	Wind-driven storm surge (m)	Wave setup/Total storm surge
Sansha	20090809 06:00	0.21	1.01	17.2%
Buoy 1	20090809 10:00	0.08	1.05	7.1%
Pingtan	20090808 14:00	0.28	0.79	24.0%
Chongwu	20090808 11:00	0.08	1.08	6.9%
Xiamen	20090808 10:00	0.05	1.54	3.1%
Dongshan	20090807 09:00	0.03	0.82	3.5%

4.5. Water level and current effects on wave

The SWH difference induced by water levels and currents was estimated by subtracting SWH results from 'SWAN only' from that of 'ADCIRC + SWAN'. Again, the scatter plots are employed to relate the SWH difference with the tidal elevation and storm surge, respectively.

Accepted manuscript

ACCEPTED MANUSCRIPT

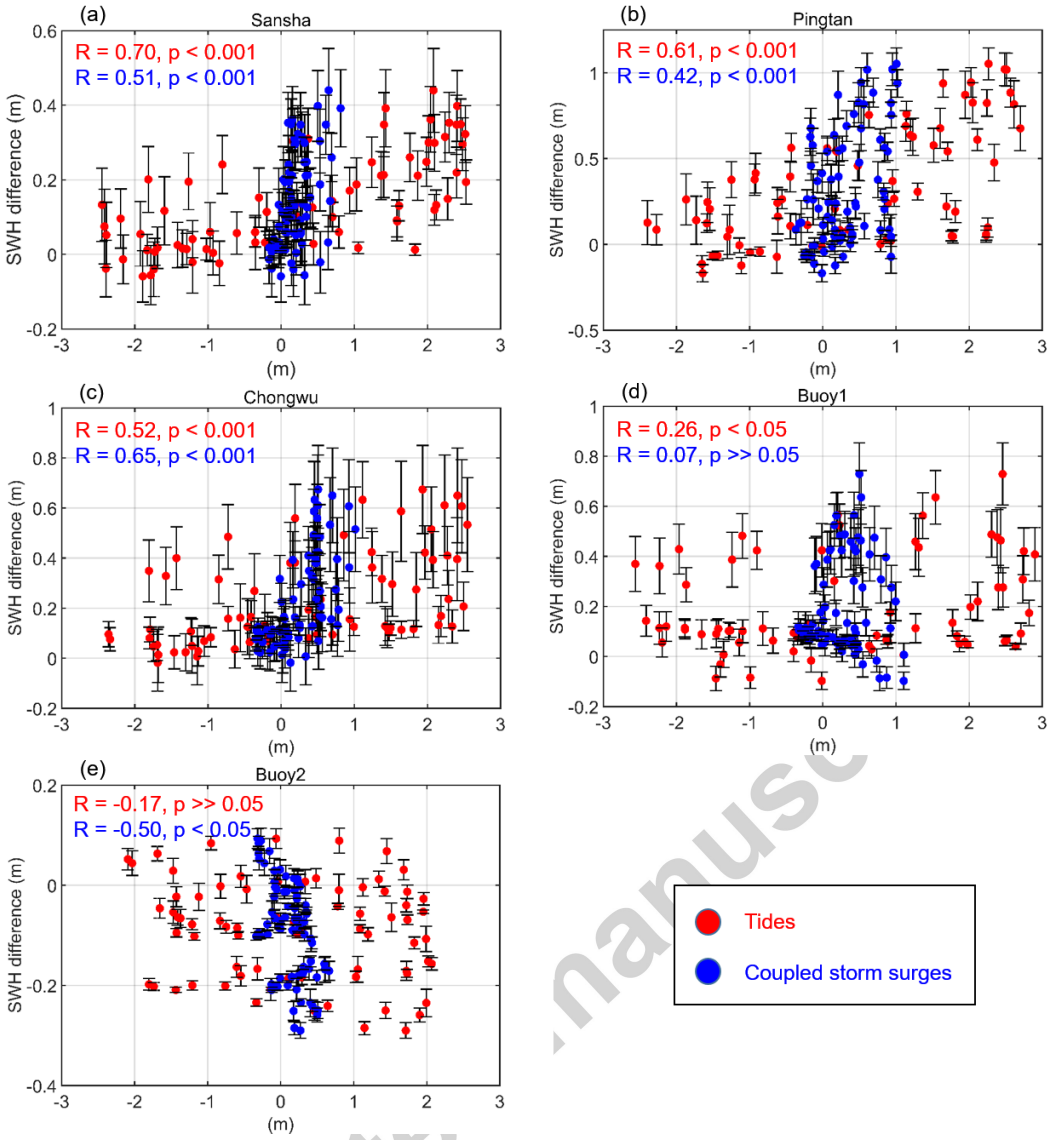

Fig. 10. Scatter plots showing the trend of SWH difference against tides (red dots) and coupled storm surges (blue dots) at regions of (a) Sansha, (b) Pingtan, (c) Chongwu, (d) Buoy 1 and (e) Buoy 2 during Morakot, The black vertical lines are error bars, indicating one standard deviation from the mean.

A systematic increase in SWH difference is observed at large values of tidal elevation in the nearshore areas (Figs. 10a-c), with statistically significant correlation coefficient (R = 0.70, 0.61, 0.52 at Sansha, Pingtan and Chongwu, respectively). Also, the SWH difference trends positively with storm surge in these regions. The SWH

difference was in a phase-locked manner with water levels inside the estuary, which indicates water levels govern wave height modulations in the nearshore areas. A large increase of wave height, about 0.5 m, occurred at Sansha during high water levels induced by tidal change and storm surge. The SWH difference at other estuary regions was also significant, with a range of -0.4 m at low water levels and 0.4 m at high water levels.

A much weaker and not significant correlation is observed at Buoy 1 (Fig. 9d). This weak correlation at Buoy 1 is likely to result from deep local water depth compared to three other stations. Additionally, the phase-locked manner failed at Buoy 2 (Fig. 9e), where a decrease of SWH occurred when ocean currents flow in the same direction with wave (not shown). It is consistent with conditions favorable for wave height decay when ocean current flows in the same direction of the wave, which is caused by the current-induced modification of wind energy input to the wave generation.

5. Conclusions

Taiwan and coastal Fujian are prone to large typhoons due to their geographic locations in the northwest Pacific. Here, the impact of wave-current interactions in the TS is investigated using a typhoon case from a simple one-way coupled ADCIRC + SWAN model.

Model results reproduced in-situ observations well, especially at our dynamical interest regions. Including the effects of wave-current interaction leads to a better agreement between model results (e.g., SWH, water levels) with observations. Strong persistent winds during Morakot induced large waves, while wave breaking generated radiation stress gradients when waves propagate into shallow surf zone. Radiation

Accepted manuscript

stress gradients subsequently result in wave setup via the transfer of momentum flux. The importance of wave setup, as compared with wind-driven storm surge, shows that wave effects can contribute up to 24% of the total storm surge. The modeled wave setup is up to 0.28 m during Typhoon Morakot. In our model, wind wave plays a critical role in shaping the wave setup in the nearshore areas. Nevertheless, it is likely that the extreme value of wave setup might be constrained by the gentle slope of bathymetry in the TS.

The SWH is sensitive to the water levels in the estuary. High water levels due to tidal change and storm surge stabilize the wind wave and decay wave breaking, and vice versa. This mechanical forcing might play an important role in the regions of strong tides, such as the TS. Outside of the estuary, the SWH difference is explained by the current-induced modification of wind energy input to the wave generation.

These results emphasize that considering effects of wave-current interaction in the circulation and wave models is needed in the TS during typhoons. Future studies should also consider other effects of wave-current interaction, such as the wave effects on surface roughness and bottom friction.

Acknowledgments. This research was funded by grants from the program of Xiamen Southern Oceanographic Center (NO.15PZB009NF05). Xiaolong Yu is supported by the China Scholarship Council for his PhD study in Southampton. We acknowledge helpful discussions with Katsiaryna Pabortsava, Rafael Jaume Catany and Jiayi Fang. We are grateful to the scientists and technicians that helped during deployment and recovery of the buoys.

Accepted manuscript

ACCEPTED MANUSCRIPT

References

Bolaños, R., Brown, J. M., Souza, A. J., 2014. Wave-current interactions in a tide dominated estuary. Cont. Shelf Res., 87, 109-123.

Bowen, A. J., Inman, D. L., Simmons, V. P., 1968. Wave 'set-down' and set-up. J. Geophys. Res., 73, 2156-2202.

Brown, J. M., Bolaños, R., Wolf, J., 2013. The depth-varying response of coastal circulation and water levels to 2D radiation stress when applied in a coupled wave-tide-surge modelling system during an extreme storm. Coast. Eng., 82, 102-113.

Cai, F., Su, X. Z., Liu, J. H., Li B., Lei G., 2009. Coastal erosion in China under the condition of global climate change and measures for its prevention. Prog. Nat. Sci., 19, 415-426.

Chang, C. P., Yeh, T. C., Chen J. M., 1993. Effects of Terrain on the Surface-Structure of Typhoons over Taiwan. Mon. Weather Rev., 121, 734-752.

Chen, D.W., 2006. Analysis and modeling study of Typhoon sea surface wind field in the vicinity of Taiwan. Master degree thesis, Xiamen University, Xiamen, Fujian, China.

Dietrich, J. C., and Coauthors, 2010. A High-Resolution Coupled Riverine Flow, Tide, Wind, Wind Wave, and Storm Surge Model for Southern Louisiana and Mississippi. Part II: Synoptic Description and Analysis of Hurricanes Katrina and Rita. Mon. Weather Rev., 138, 378-404.

Dietrich, J. C., and Coauthors, 2011. Modeling hurricane waves and storm surge using integrally-coupled, scalable computations. Coast. Eng., 58, 45-65.

Egbert, G. D., Erofeeva, S. Y., 2002. Efficient inverse modeling of barotropic ocean tides. J. Atmos. Ocean. Technol. 19, 183-204.

Accepted manuscript

ACCEPTED MANUSCRIPT

Fang, G. H., Kwok, Y. K., Yu, K. J., Zhu, Y. H., 1999. Numerical simulation of principal tidal constituents in the South China Sea, Gulf of Tonkin and Gulf of Thailand. Cont. Shelf Res., 19, 845-869.

Fang, J. Y., Liu, W., Yang, S. N., Brown, S., Nicholls, R. J., Hinkel, J., Shi, X. W., Shi, P. J., 2017. Spatial-temporal changes of coastal and marine disasters risks and impacts in Mainland China. Ocean & Coastal Management, 139, 125-140.

Feng, X. R., Yin, B. S., Yang, D. Z., 2012. Effect of hurricane paths on storm surge response at Tianjin, China. Estuar., Coast. Shelf Sci., 106, 58-68.

Feng, X. R., Yin, B. S., Yang, D. Z., 2016. Development of an unstructured-grid wave-current coupled model and its application. Ocean Model., 104, 213-225.

Fujii, T., Mitsuta, Y., 1986. Synthesis of a Stochastic Typhoon Model and Simulation of Typhoon Winds. Annuals Disaster Prevention Research Institute, Kyoto University, 29(B-1), 229-239 (in Japanese).

Fujita, T., 1952. Pressure Distribution Within Typhoon. Geophys. Mag., 23, 437 – 451.

Funakoshi, Y., Hagen, S. C., Bacopoulos, P., 2008. Coupling of Hydrodynamic and Wave Models: Case Study for Hurricane Floyd (1999) Hindcast. J. Waterway, Port, Coastal, Ocean Eng., 134, 321-335.

González, F. I., 1984. A Case Study of Wave-Current-Bathymetry Interactions at the Columbia River Entrance. J. Phys. Oceanogr., 14, 1065-1078.

Hong, H. S., Chai, F., Zhang, C. Y., Huang, B. Q., Jiang, Y. W., Hu, J. Y., 2011. An overview of physical and biogeochemical processes and ecosystem dynamics in the Taiwan Strait. Cont. Shelf Res., 31, S3-S12.

Hopkins, J., Elgar, S., Raubenheimer, B., 2016. Observations and model simulations of wave-current interaction on the inner shelf. J. Geophys. Res., 121, 198-208.

Accepted manuscript

ACCEPTED MANUSCRIPT

Hu, C. K., Chiu, C. T., Chen, S. H., Kuo, J. Y., Jan, S., Tseng, Y. H., 2010. Numerical Simulation of Barotropic Tides around Taiwan. Terr. Atmos. Ocean Sci., 21, 71-84.

Huang, Y., Weisberg, R. H., Zheng, L. Y., 2010. Coupling of surge and waves for an Ivan-like hurricane impacting the Tampa Bay, Florida region. J. Geophys. Res., 115, C12009.

Jan, S., Chern, C. S., Wang, J., 2002. Transition of tidal waves from the East to South China Seas over the Taiwan Strait: Influence of the abrupt step in the topography. J. Oceanogr., 58, 837-850.

Jan, S., Chern, C. S., Wang, J., Chao, S. Y., 2004. The anomalous amplification of M2 tide in the Taiwan Strait. Geophys. Res. Lett., 31, L07308.

Kim, S. Y., Yasuda, T., Mase, H., 2010. Wave set-up in the storm surge along open coasts during Typhoon Anita. Coast. Eng., 57, 631-642.

Liu, W. C., Huang, W. C., Chen, W. B., 2016. Modeling the interaction between tides and storm surges for the Taiwan coast. Environ. Fluid Mech., 16, 721-745.

Longuet-Higgins, M. S., Stewart, R. W., 1962. Radiation stress and mass transport in gravity waves, with application to 'surf beats'. J. Fluid Mech., 13, 481- 504.

Longuet-Higgins, M. S., Stewart, R. W., 1964. Radiation stresses in water waves; a physical discussion, with applications. Deep-Sea Res., 11, 529-562.

Malhadas, M. S., Leitao, P. C., Silva, A., Neves, R., 2009. Effect of coastal waves on sea level in Óbidos Lagoon, Portugal. Cont. Shelf Res., 29, 1240-1250.

Miyazaki, M., Ueno, T., Unoki, S., 1961. Theoretical investigations of typhoon surges along the Japanese coast. Oceanogr. Mag. 13, 51-75.

Olabarrieta, M., Warner, J. C., Kumar, N., 2011. Wave-current interaction in Willapa Bay. J. Geophys. Res., 116, C12014.

Accepted manuscript

ACCEPTED MANUSCRIPT

Pawlowicz, R., Beardsley, B., Lentz, S., 2002. Classical tidal harmonic analysis including error estimates in MATLAB using T_TIDE. Comput. Geosci. 28, 929-937.

Raubenheimer, B., Guza, R. T., Elgar, S., 2001. Field observations of wave-driven setdown and setup. J. Geophys. Res., 106, 4629-4638.

Resio, D. T., Westerink, J. J., 2008. Modeling the physics of storm surges. Phys. Today, 61, 33-38.

Roland, A., and Coauthors, 2009. On the development and verification of a 2-D coupled wave-current model on unstructured meshes. J. Marine Syst., 78, S244-S254.

Shimada, T., Chang, Y., Lan, K. W., 2016. Climatological features of surface winds blowing through the Taiwan Strait. Int. J. Climatol., 36, 4287-4296.

Smith, J. A., 2006. Wave-current interactions in finite depth. J. Phys. Oceanogr., 36, 1403-1419.

Wei, C. C., 2015. Forecasting surface wind speeds over offshore islands near Taiwan during tropical cyclones: Comparisons of data-driven algorithms and parametric wind representations. J. Geophys. Res., 120, 1826-1847.

Wolf, J., Prandle, D., 1999. Some observations of wave-current interaction. Coast. Eng., 37, 471-485.

Yu, H. Q., Yu, H. M., Wang, L., Kuang, L., Wang, H., Ding, Y., Ito, S., Lawen, J., 2017. Tidal propagation and dissipation in the Taiwan Strait. Cont. Shelf Res., 136, 57-73.

Zhang, W. Z., Hong, H. S., Shang, S. P., Yan, X. H., Chai, F., 2009. Strong southward transport events due to typhoons in the Taiwan Strait. J. Geophys. Res., 114, C11013.

Accepted manuscript

ACCEPTED MANUSCRIPT

Zhang, W. Z., Shi, F. Y., Hong, H. S., Shang, S. P., Kirby, J. T., 2010. Tide-surge Interaction Intensified by the Taiwan Strait. J. Geophys. Res., 115, C06012.

Highlights

- Wave setup can contribute up to 24% of the total storm surge in the Taiwan Strait during Typhoon Morakot.
- The wave contribution is strongly determined by wind field and the slope of the sea floor.
- Water levels are to leading order in modulating significant wave height inside the estuary.
- Wave-current interactions should be considered in the study area for a typhoon forecast.

Accepted manuscript